



Title	Crystal structures, magnetic properties, and DFT calculation of B-site defected 12L-perovskites Ba <sub>2</sub> La <sub>2</sub> MW <sub>2</sub> O <sub>12</sub> (M = Mn, Co, Ni, Zn)
Author(s)	Doi, Yoshihiro; Wakeshima, Makoto; Tezuka, Keitaro; Shan, Yue Jin; Ohoyama, Kenji; Lee, Sanghyun; Torii, Shuki; Kamiyama, Takashi; Hinatsu, Yukio
Citation	Journal of physics : condensed matter, 29(36), 365802 <a href="https://doi.org/10.1088/1361-648X/aa7c9b">https://doi.org/10.1088/1361-648X/aa7c9b</a>
Issue Date	2017-09-13
Doc URL	<a href="http://hdl.handle.net/2115/71453">http://hdl.handle.net/2115/71453</a>
Rights	This is an author-created, un-copyedited version of an article published in Journal of Physics: Condensed Matter. IOP Publishing Ltd is not responsible for any errors or omissions in this version of the manuscript or any version derived from it. The Version of Record is available online at 10.1088/1361-648X/aa7c9b.
Type	article (author version)
Additional Information	There are other files related to this item in HUSCAP. Check the above URL.
File Information	JPCM29 365802.pdf



[Instructions for use](#)

**Crystal structures, magnetic properties, and DFT calculation  
of B-site defected 12L-perovskites  $\text{Ba}_2\text{La}_2\text{MW}_2\text{O}_{12}$  (M = Mn,  
Co, Ni, Zn)**

**Yoshihiro Doi\*<sup>1</sup>, Makoto Wakeshima<sup>1</sup>, Keitaro Tezuka<sup>2</sup>, Yue Jin Shan<sup>2</sup>, Kenji  
Ohoyama<sup>3</sup>, Sanghyun Lee<sup>4</sup>, Shuki Torii<sup>4</sup>, and Takashi Kamiyama<sup>4</sup>, and Yukio  
Hinatsu<sup>1</sup>**

<sup>1</sup> Graduate School of Science, Hokkaido University, Sapporo, Hokkaido 060-0810,  
Japan

<sup>2</sup> Graduate School of Engineering, Utsunomiya University, Utsunomiya, Tochigi  
321-8585, Japan

<sup>3</sup> Graduate School of Science and Engineering, Ibaraki University, Mito, Ibaraki  
310-8512, Japan

<sup>4</sup> High Energy Accelerator Research Organization (KEK), Tsukuba, Ibaraki 305-0801,  
Japan

\*Corresponding Author: Yoshihiro Doi

Graduate School of Science,  
Hokkaido University,  
Sapporo, Hokkaido 060-0810, Japan.  
TEL: +81-11-706-2715  
FAX: +81-11-706-4931  
E-mail: [doi@sci.hokudai.ac.jp](mailto:doi@sci.hokudai.ac.jp)

## Abstract

The synthesis, crystal structures and magnetic properties of  $\text{Ba}_2\text{La}_2\text{MW}_2\text{O}_{12}$  ( $\text{M} = \text{Mn}, \text{Co}, \text{Ni}, \text{Zn}$ ) were investigated. They crystallize in the 12-layer polytype of the perovskite structure with a regular cation defect in the B-site. The results of neutron diffraction measurements reveal that they adopt a rhombohedral structure with a space group  $R\bar{3}$  and have a cation ordering between Ba and La ions in the A-site. In these compounds, the magnetic M ions form the two-dimensional triangular lattice. From the results of magnetic measurements, the ferromagnetic ordering of  $\text{M}^{2+}$  ions for  $\text{M} = \text{Co}$  ( $T_C = 1.3 \text{ K}$ ) and Ni (6.2 K) and the paramagnetic behavior ( $T > 1.8 \text{ K}$ ) with an antiferromagnetic interaction for  $\text{M} = \text{Mn}$  are observed. From the DFT calculation, their band structures and magnetic interactions are discussed.

**Keywords:** B-site defected 12L-perovskite, Triangular lattice, Cation ordering, Neutron diffraction, DFT calculation, Magnetic interaction

## Introduction

Low-dimensional magnetic materials have attracted a great deal of interest because of their anomalous magnetic properties at low temperatures. In particular, the antiferromagnetism on the two-dimensional triangular lattice have been extensively studied from the aspects of geometrical frustration [1, 2] and quantum spin liquid [3, 4]. In order to find further interesting magnetic behaviors, it is absolutely essential to explore new compounds with a triangular arrangement of magnetic ions.

For such a purpose, we have previously investigated the crystal structures and magnetic properties of 6L-Ba<sub>3</sub>MSb<sub>2</sub>O<sub>9</sub> (M = Mn, Co, Ni) [5]. They have polymorphic crystal structures of perovskite [6, 7], in which there exist two-dimensional layers containing a triangle array of M ions and each layer is magnetically separated by the diamagnetic layers containing Sb<sup>5+</sup> ions. Reflecting these features, the 6L-Ba<sub>3</sub>MSb<sub>2</sub>O<sub>9</sub> (6H-A phase) behave as two-dimensional antiferromagnets at low temperatures [5]. In recent years, magnetic studies of related compounds have been extensively spread [8, 9], and the spin liquid state was found in the related 6H-B phases with a different stacking sequence of triangular lattices along the *c*-axis [10, 11].

In this study, we have focused our attention on the B-site defected 12L-perovskites A<sub>4</sub>MM'<sub>2</sub>O<sub>12</sub> (A = Ba, Sr, La; M = transition metal, lanthanide etc.; M' = W, Re) [12-27].

This crystal structure can be understood by replacing one M' ion with vacancy from a perovskite polymorph 12L-perovskite  $A_4MM'_3O_{12}$  such as 12L-Ba<sub>4</sub>LnM'<sub>3</sub>O<sub>12</sub> (Ln = lanthanides; M' = Ru, Ir) [28-30]. This crystal structure has a triangular lattice of M ions similar to 6L-Ba<sub>3</sub>MSb<sub>2</sub>O<sub>9</sub> (6H-A and 6H-B) [5, 11] but with a different stacking sequence. In addition, the shorter M–M distance ( $a \sim 5.7 \text{ \AA} < a \sim 5.9 \text{ \AA}$ ) and longer interlayer distance ( $c/3 \sim 9.1 \text{ \AA} > c/2 \sim 7.2 \text{ \AA}$ ) than 6L-Ba<sub>3</sub>MSb<sub>2</sub>O<sub>9</sub> are considered to be more adequate for the two-dimensional magnet. However, the investigation on the magnetic properties of  $A_4MM'_2O_{12}$  have been quite limited except for Ba<sub>2</sub>La<sub>2</sub>MnW<sub>2</sub>O<sub>12</sub> [24] and  $A_4MM'_2O_{12}$  (A = Ba, Sr, La; M = Co, Ni, Mn; M' = W, Re) [27]. On the other hand, some different structural models (the symmetry, A-site ordering/disordering, and tilting in the connection between MO<sub>6</sub> and M'O<sub>6</sub> octahedra, etc.) have been reported for the  $A_4MM'_2O_{12}$  compounds [12-27].

In order to elucidate the detailed crystal structures and magnetic properties of 12L-perovskites  $A_4MM'_2O_{12}$ , we selected the Ba<sub>2</sub>La<sub>2</sub>MW<sub>2</sub>O<sub>12</sub> (M = Co, Mn, Ni, Zn) [17, 18, 24, 25, 27] containing magnetic M cations and two kinds of A cations (Ba and La). Some results about magnetic measurements are common to a recent work by Rawl et al. [27]; thus, in this paper, we will mainly report the crystal structure determined by the neutron diffraction measurements, and results of additional analysis of magnetic

data and DFT calculations in detail.

## Experimental

### Sample preparation

The title compounds  $\text{Ba}_2\text{La}_2\text{MW}_2\text{O}_{12}$  were prepared as polycrystalline samples by the solid-state reaction. For  $M = \text{Co}, \text{Ni}, \text{Zn}$  samples,  $\text{BaCO}_3$ ,  $\text{La}_2\text{O}_3$  (dried at  $900^\circ\text{C}$ , 12 h),  $\text{CoO}$ ,  $\text{NiO}$ ,  $\text{ZnO}$  and  $\text{WO}_3$  were used as starting materials. The mixture with the stoichiometric metal ratio was pressed into pellets, and heated at  $900^\circ\text{C}$  12 h,  $1100^\circ\text{C}$  12 h, and  $1200^\circ\text{C}$  12 h  $\times$  2-3 with intermediate grindings and pelletizings. For  $M = \text{Mn}$  sample,  $\text{BaO}$ ,  $\text{La}_2\text{O}_3$  (dried),  $\text{MnO}$ , and  $\text{WO}_3$  were mixed and enclosed in a platinum tube in the glove box filled with Ar gas, and then it was sealed in an evacuated silica ampoule. This ampoule was heated at  $1200^\circ\text{C}$  3 h and then quenched by the liquid nitrogen. These samples contain small amounts ( $M = \text{Mn}$ : 2.8 wt%;  $\text{Co}$ : 1.2;  $\text{Ni}$ : 0.4;  $\text{Zn}$ : 0.2) of impurity phase ( $\text{BaWO}_4$ ).

### Powder x-ray and neutron diffraction measurements

The powder x-ray diffraction (XRD) measurements were performed at room

temperature in the range  $10^\circ \leq 2\theta \leq 120^\circ$  using a  $2\theta$  step size of  $0.02^\circ$  with Cu-K $\alpha$  radiation on a Rigaku MultiFlex diffractometer. In addition, powder neutron diffraction (ND) profiles were collected at room temperature. For M = Ni, the ND measurement (the neutron wavelength  $\lambda = 1.84843 \text{ \AA}$ ) was performed by HERMES [31], installed at the JRR-3M reactor in Japan Atomic Energy Agency (JAEA), Tokai. For M = Zn, the time-of flight neutron diffraction (TOF-ND) by Super HRPD (BL08), installed at the Material and Life Science Experimental Facility (MLF) of the Japan Proton Accelerator Research Complex (J-PARC). All the data were analyzed by the Rietveld technique by using the program RIETAN-FP [32] for both XRD and ND, and the Z-code program package [33, 34] for the TOF-ND. The crystal and magnetic structures were drawn by the VESTA program [35].

#### *Magnetic susceptibility and specific heat measurements*

Magnetic measurements were carried out by a SQUID magnetometer (Quantum Design, MPMS-5S). The temperature dependence (1.8–400 K) of magnetic susceptibility was performed in both zero-field-cooled (ZFC) and field-cooled (FC) conditions, and the field dependence (0–9 T) of magnetization was also measured at 1.8 K.

The specific heat measurements were carried out in the temperature range 1.8–300 K by using a relaxation technique with a commercial physical property measurement system (Quantum Design, PPMS) in an applied field of 0 or 5 T. The sintered sample in the form of a pellet was mounted on a thin alumina plate with Apiezon N grease for better thermal contact.

#### DFT calculation and UV-vis diffuse reflectance spectra

Calculations of the electronic structure and the density of states (DOS) were performed using the WIEN2k program package [36]. This program employs the full-potential linearized augmented plane wave + local orbitals (FP-LAPW+lo) method based on density functional theory (DFT). We used the modified Becke-Johnson (mBJ) exchange potential + local density approximation (LDA)-correlation [37]. In the calculations, the convergence parameter was set to be  $R_{\text{MT}}k_{\text{max}}=7.0$ , and the muffin-tin (MT) spheres are  $R_{\text{MT}}$  (in unit of bohr) = 2.39~2.50 (for Ba), 2.41~2.50 (La), 2.20 (Mn), 1.98 (Ni), 2.11 (Zn), 1.77~1.86 (W), and = 1.52 ~ 1.60 (O). We used  $10 \times 10 \times 10$  meshes with 170 k points in the first Brillouin zone. Some illustrations for the spin density distribution are drawn by the VESTA program [35]. In order to compare calculated and optical band gaps, UV-vis diffuse reflectance spectra were measured with

a V-570 instrument (JASCO).

## Results and discussion

### Synthesis and crystal structure

The  $\text{Ba}_2\text{La}_2\text{MW}_2\text{O}_{12}$  (M = Mn, Co, Ni, and Zn) compounds were prepared as the perovskite-related phase. The XRD profiles are shown in Fig. 1 (M = Ni and Zn) and Fig. S1 (Mn and Co). They are well indexed by a hexagonal unit cell ( $a = \sim 5.7 \text{ \AA}$ ,  $c = \sim 27.4 \text{ \AA}$ ) with a rhombohedral symmetry, and corresponding to earlier reports for  $\text{Ba}_2\text{La}_2\text{MW}_2\text{O}_{12}$  compounds [17, 18, 24, 25, 27]. In these reports, the space group  $R\text{-}3m$  (No. 166) was applied for the structural analysis (Table S1). The Rietveld analysis of XRD data using this  $R\text{-}3m$  model apparently gives a good result; however, we have used a different model with the space group  $R\text{-}3$  (No. 148) based on the results of neutron diffraction measurements as will be described below. The refined parameters determined by XRD are listed in Table S2.

In order to obtain more detailed structural information of  $\text{Ba}_2\text{La}_2\text{MW}_2\text{O}_{12}$  such as the space group, ordered/disordered arrangement of Ba/La ions, and possibility of oxygen ion defects, we have performed the neutron diffraction measurements for M =

Ni and Zn compounds. Fig. 2 shows the ND profile of  $\text{Ba}_2\text{La}_2\text{NiW}_2\text{O}_{12}$  at room temperature. We first tried to analyze the data by using the  $R-3m$  space group as a starting structural model; however, this trial ended in failure because of the significant disagreement between observed and calculated peak intensities although each calculated Bragg peaks were appropriately located at observed peak positions. This result indicates that  $\text{Ba}_2\text{La}_2\text{NiW}_2\text{O}_{12}$  has a different symmetry or atomic positions. From this aspect, we tested the subgroups of  $R-3m$  for the structural analysis and finally found that the space group  $R-3$  (No. 148) is adequate. The calculated profile of the  $R-3$  model is plotted in Fig. 2 and shows a good agreement with the observed profile. The refined structural parameters are listed in Table 1. This model is also used for the analysis of isostructural 12L-perovskites  $\text{A}_3\text{LaNb}_3\text{O}_{12}$  ( $\text{A} = \text{Sr}, \text{Ba}$ ) [38] and  $\text{Sr}_3\text{NdNb}_{3-x}\text{Ti}_x\text{O}_{12-\delta}$  [39]. The specific difference between these two models is that anions (O1 and O2) occupy different crystallographic sites. In contrast, those of metal sites are almost unchanged (*cf.* Tables 1 and S2). Fig. 3 shows the comparison of these models for XRD and ND calculated profiles. For the XRD measurements, both models bring about similar calculation profiles since the atomic scattering factor of oxygen ion is much smaller than those of metal ions in  $\text{Ba}_2\text{La}_2\text{MW}_2\text{O}_{12}$ . The  $R-3$  model is well supported by the TOF-ND measurement for  $\text{M} = \text{Zn}$  shown in Fig. 4. From the Rietveld analysis of both

ND and TOF-ND data, the  $\text{Ba}^{2+}$  and  $\text{La}^{3+}$  ions adopt fully ordered arrangement unlike some earlier reports [18, 25, 27] (see Fig. S2) and there are no oxygen defects within the standard deviation. The structural parameters for Ni and Zn compounds are summarized in Table 1.

Fig. 5(a) illustrates the schematic crystal structure of  $\text{Ba}_2\text{La}_2\text{MW}_2\text{O}_{12}$ . In this structure, M and W ions occupy different octahedral sites, and these octahedra connect with each other by sharing the corner oxygen ion. They construct a perovskite (or a double-perovskite like) block in  $ab$  plane. The La and Ba ions locate in this block and between blocks, respectively. The connection of  $\text{MO}_6$  and  $\text{WO}_6$  is slightly tilted due to the loss of mirror planes in the  $R-3$  structure shown in Fig. 5. In the view of magnetism, the magnetic M ions form a triangular lattice in  $ab$  plane. This lattice stacks along the  $c$  axis with a translational operation  $(+2/3, +1/3, +1/3)$  reflecting a rhombohedral symmetry.

The bond lengths calculated by the obtained structural parameters are summarized in Table 2. The bond valence sums (BVSs) are also calculated and shown in this table. The BVS values suggest that the valence states of cations are represented as  $\text{Ba}^{2+}_2\text{La}^{3+}_2\text{M}^{2+}\text{W}^{6+}_2\text{O}_{12}$ .

### Magnetic properties

#### (i) Magnetic susceptibilities of $\text{Ba}_2\text{La}_2\text{MW}_2\text{O}_{12}$ (M = Mn, Co, Ni)

Fig. 6 shows the temperature dependence of the inverse magnetic susceptibilities ( $\chi_M^{-1}$ ) for  $\text{Ba}_2\text{La}_2\text{MW}_2\text{O}_{12}$  (M = Mn, Co, Ni). The ZFC data above 150 K were fitted by the Curie-Weiss law, and obtained effective magnetic moments ( $\mu_{\text{eff}}$ ) and Weiss constants ( $\theta$ ) are listed in Table 3. The  $\mu_{\text{eff}}$  values for M = Mn and Ni compounds are close to the spin only values of  $\text{M}^{2+}$  ion ( $\mu_{\text{M}^{2+}}$ ). On the other hand, for M = Co the  $\mu_{\text{eff}}$  is much larger than  $\mu_{\text{M}^{2+}} = 3.87 \mu_B$  ( $3d^7$ ;  $S = 3/2$ ) which is attributed to the orbital angular momentum derived from the degeneracy of  $t_{2g}$  orbital [40]. The Weiss constants ( $\theta_{\text{LT}}$ ) were also calculated by using lower temperature data below 30 K (Table 3), which is for excluding the influence from the slight curvature of  $\chi_M^{-1}$  vs  $T$  plot due to the magnetic excited state and crystal field effect, etc. The negative (M = Mn) and positive (Co and Ni)  $\theta_{\text{LT}}$  values suggest that the dominant magnetic interaction between  $\text{M}^{2+}$  ions are antiferromagnetic and ferromagnetic, respectively.

#### (ii) Magnetic transition of $\text{Ba}_2\text{La}_2\text{MnW}_2\text{O}_{12}$

The temperature dependence of specific heat and the field dependence of magnetization at 1.8 K for  $\text{Ba}_2\text{La}_2\text{MnW}_2\text{O}_{12}$  are plotted in Figs. 7 and 8, respectively. In

this compound, the magnetic transition was not observed down to 1.8 K. The specific heat divided by temperature ( $C_p/T$ ) shows an upturn with decreasing temperature in contrast to the data of diamagnetic  $\text{Ba}_2\text{La}_2\text{ZnW}_2\text{O}_{12}$ . This result suggests an onset of magnetic transition occurs at lower temperatures. The magnetization at 1.8 K varies linearly against the magnetic field and does not saturate even at 5 T, which indicates that the magnetic ground state is antiferromagnetic. These results are corresponding to an antiferromagnetic transition at 1.7 K determined by Rawl et al. [27].

(iii) Magnetic transition of  $\text{Ba}_2\text{La}_2\text{CoW}_2\text{O}_{12}$

Fig. 9 represents the temperature dependence of specific heat for the Co compound in an applied field of 0 and 5 T. A sharp anomaly is observed at 1.3 K indicating the occurrence of long-range magnetic ordering, and this anomaly is broadened and shifted to 5 K by applying the magnetic field. This result suggests that the observed anomaly is attributed to not an antiferromagnetic transition but a ferromagnetic one. In fact, the field dependence of magnetization (Fig. 8) shows a rapid increasing in a small magnetic field region and a saturation behavior ( $2.2 \mu_B$ ) above  $\sim 2$  T. In order to obtain further information of this transition, the temperature dependence of magnetic entropy ( $S_{\text{mag}}$ ) is calculated and plotted in Fig. 9. Here, the  $S_{\text{mag}}$  is obtained by

$S_{\text{mag}} = \int (C_p - C_{\text{lat}})/T dT$  in which the  $C_{\text{lat}}$  means the lattice contribution of specific heat and the specific heat data of  $\text{Ba}_2\text{La}_2\text{ZnW}_2\text{O}_{12}$  are used for this contribution. Above  $\sim 5$  K the  $S_{\text{mag}}$  is converged to  $5.5 \text{ J mol}^{-1} \text{ K}^{-1}$ , which is close to  $R \ln 2 = 5.76 \text{ J mol}^{-1} \text{ K}^{-1}$  ( $R$ : gas constant). This result indicates that the ground doublet state of  $\text{Co}^{2+}$  ion brings about this ferromagnetic transition.

(iv) Magnetic transition of  $\text{Ba}_2\text{La}_2\text{NiW}_2\text{O}_{12}$

The temperature dependence of specific heat for Ni compound is plotted in Fig. 10, and an anomaly is found at 6.2 K. This anomaly agrees with the magnetic transition observed in the inverse magnetic susceptibility (inset in Fig. 6). Thus, the ferromagnetic ordering of  $\text{Ni}^{2+}$  ions occurs below  $T_C = 6.2$  K. From the magnetization measurement (Fig. 8), it is found that this compound shows a magnetic hysteresis loop with a residual magnetization of  $1.25 \mu_B$  and gradual increasing toward  $2 \mu_B$ . The temperature dependence of  $S_{\text{mag}}$  is calculated by the same way as Co compound and is also plotted in Fig. 10. The change of  $S_{\text{mag}}$  due to this ferromagnetic transition is determined to be  $8.90 \text{ J mol}^{-1} \text{ K}^{-1}$ . This value is close to  $R \ln 3 = 9.13 \text{ J mol}^{-1} \text{ K}^{-1}$  expected from the  $S = 1$  ion with a spin degeneracy  $2S + 1$ ; therefore the magnetic moments of  $\text{Ni}^{2+}$  ions are fully ordered at 1.8 K. The characteristic shape of  $M-H$  curve and smaller residual

magnetization than  $2 \mu_B$  may be due to the single-ion anisotropy of  $Ni^{2+}$  ion by using a polycrystalline sample.

### UV-vis diffuse reflectance spectra

Fig. 11 shows the UV-vis diffuse reflectance spectra of  $Ba_2La_2ZnW_2O_{12}$  and  $Ba_2La_2NiW_2O_{12}$ . The absorption values were calculated from the reflectance data using the Kubelka Munk function given by

$$F(R_\infty) = \frac{(1 - R_\infty)^2}{2R_\infty}, \quad (1)$$

where  $R_\infty$  is the reflectance [41]. The energy of the optical band gap was determined using the Tauc plot [42]. In these compounds, the photon energy ( $h\nu$ ) is proportional to  $(F(R_\infty)h\nu)^2$  near the bottom of the conduction band. The optical band gaps for  $M = Zn$  and  $Ni$  compounds were determined to be 3.75 and 2.25 eV, respectively. For the latter compound, two additional peaks were observed around 3 eV in the Tauc plot.

### DFT calculation

#### (i) $Ba_2La_2ZnW_2O_{12}$

In order to verify the electronic structure of  $Ba_2La_2MW_2O_{12}$  ( $M = Mn, Ni, Zn$ ), we carried out the mBJ + LDA calculations. Fig. 12 displays the energy dispersions and the

total and partial densities of states (DOSs) for  $\text{Ba}_2\text{La}_2\text{ZnW}_2\text{O}_{12}$ . The occupied and unoccupied bands form a band gap of 3.0 eV around the Fermi level ( $E_F$ ). This value is smaller than the optical band gap of the UV-vis spectra, and this underestimation is generally shown in the DFT calculation.

The valence bands (VBs) of  $\text{Ba}_2\text{La}_2\text{ZnW}_2\text{O}_{12}$  demonstrates the hybridization between Zn 3d and O2 2p states over the broad range from  $-3.7$  eV to  $E_F$ . Below them, there exist further VBs dominated by the O 2p states; but the bonding orbital-like W 5d states are also situated in the same VBs indicating the W 5d – O 2p hybridization. Such bonding orbital-like 5d states are often found in hexavalent W oxides [43-45]. On the other hand, the bottom of conduction bands (CBs) in the narrow range from 3.0 to 3.8 eV mainly consists of W 5d and O1, O2 2p states. The dispersions reveal that the bottoms of CBs and the tops of VBs are located at the same points (L and F). This matching suggests that the ligand to metal charge transfer (LMCT)-type direct allowed transition ( $L \rightarrow L$  and/or  $F \rightarrow F$ ) is predominant for the optical band gap observed in the UV-vis spectra.

(ii)  $\text{Ba}_2\text{La}_2\text{MnW}_2\text{O}_{12}$

Fig. 13 displays the total DOS and the partial DOSs of total electrons of Ba, La, Mn, W, and O for  $\text{Ba}_2\text{La}_2\text{MnW}_2\text{O}_{12}$ . The rigid and narrow VBs are formed from Mn

spin-up 3d states from -1.4 eV to  $E_F$  and the CBs mainly consist of the W 5d and O1, O2 2p states between 0.8 to 1.9 eV; thus, the band gap is estimated to be 0.8 eV. Below the VBs of Mn spin-up states, there exist VBs consisting of O2 2p states between -5.8 and -2.6 eV and those consisting of W 5d and O 2p states between -6.1 and -8.3 eV.

The results of DOSs reveal that the Mn ion is in the divalent state with the high-spin configuration because all the Mn spin-up 3d states are located below  $E_F$  and the spin-down 3d states exist above 2.5 eV. The spin-polarized Mn 3d states and the O2 2p states hybridize with each other, and this hybridization yields very small spin polarizations of O2 2p states and W 5d states via O2, resulting in the reduction of Mn moments ( $4.2 \mu_B$ ). The spin density distribution around the central Mn ion and its ligands O2 is depicted in Fig. 13(c). The spin distribution for Mn 3d is isotropic and has spherical symmetry originated from the half-filled 3d states.

(iii)  $\text{Ba}_2\text{La}_2\text{NiW}_2\text{O}_{12}$

Figure 14 displays the total DOS and the partial DOSs of total electrons of Ba, La, Ni, W, and O for  $\text{Ba}_2\text{La}_2\text{NiW}_2\text{O}_{12}$ . The energy dispersions are shown in Fig. S3. The VBs consist of the Ni 3d states from -1.3 eV to  $E_F$  and the CBs are mainly formed from the W 5d and O1, O2 2p states between 1.5 to 2.5 eV. These bands form a band gap of 1.5 eV around the Fermi level. This value is smaller than the optical band gap (2.25 eV)

obtained from the UV-vis spectrum as with the case of  $\text{Ba}_2\text{La}_2\text{ZnW}_2\text{O}_{12}$ . The gap arises from the LMCT-type direct transition at the L and/or F points (Fig. S2).

Below the narrow VBs (Ni 3d states) from -1.3 eV to  $E_F$ , the bands consisting of O 2p states are located from -4.8 to -1.6 eV. The forbidden bandwidth (0.3 eV) between them significantly decreases as compared to that for  $\text{Ba}_2\text{La}_2\text{MnW}_2\text{O}_{12}$  (1.2 eV). This decreasing causes an enhancement of hybridization between the M 3d states and O 2p states and broadens 3d bands. The 3d bands for  $\text{Ba}_2\text{La}_2\text{NiW}_2\text{O}_{12}$  below  $E_F$  are slightly broader as compared with those of 3d bands for  $\text{Ba}_2\text{La}_2\text{MnW}_2\text{O}_{12}$ , and the contribution of O 2p states to the DOSs increase.

The partial DOSs in Fig. 14(b) show that all the spin-up 3d states and the  $t_2$ -like spin-down 3d states exist below the  $E_F$  level, and that the remaining  $e$ -like spin-down 3d states locate at around 3.2 eV. In fact, two peaks around 3 eV are observed in the UV-vis spectrum (Fig. 11), and they are considered to correspond with the Ni d-d transition from the  $t_2$  to  $e$  bands. These results also reveal that the Ni ion is in the divalent state. This compound has the magnetic moments of  $1.8 \mu_B$  per Ni atom and the magnetic moment is slightly smaller than the theoretical one because of the same reason for  $\text{Ba}_2\text{La}_2\text{MnW}_2\text{O}_{12}$ . The spin density distribution around the central Ni ion and its

ligands O2 is depicted in Fig. 14(c) and the distribution for Ni 3d expands toward O2 sites, indicating that the spin density consists of the spin-up  $3d_{x^2-y^2}$  and  $3d_{3z^2-r^2}$  states.

(iv) Summary of band structures of  $Ba_2La_2MW_2O_{12}$

The band structures of  $Ba_2La_2MW_2O_{12}$  are summarized as follows. In general, the energy difference between M 3d and O 2p bands decreases with increasing the atomic number of M with the same valence. The energy schemes are depicted in Fig. 15. The M 3d bands are split by the effect of crystalline field and d-d coulombic repulsion. The hybridization between M 3d and O 2p states broaden the M 3d bands, and the hybridization increases in the order of Mn, Co, Ni, and Zn.

Discussion about magnetic interaction in  $Ba_2La_2MW_2O_{12}$  ( $M = Mn, Co, Ni$ )

The magnetic transition temperature of  $Ba_2La_2NiW_2O_{12}$  is higher than that of  $Ba_2La_2MnW_2O_{12}$ , and the inversion of sign of the magnetic interaction ( $J$ ) occurs. In general, the superexchange interaction strongly depends on  $S$  (magnetic moment),  $U$  (d-d coulombic repulsion energy),  $\Delta$  (charge transfer energy), and  $t$  (ligand p-metal d hybridization strength). For the  $180^\circ$  superexchange interaction pathway, the super exchange integral ( $J$ ) is represented by the following equation [46],

$$J = \left( \frac{t^2}{S\Delta} \right)^2 \left( \frac{2}{2\Delta + U_p} + \frac{1}{U} \right) \sim \left( \frac{t^2}{S\Delta} \right)^2 \left( \frac{1}{\Delta} + \frac{1}{U} \right). \quad (2)$$

This Zaanen-Sawatzky model is in good agreement with the experimental results for NaCl-type MO (M = Mn, Fe, Co, Ni). For the more general pathway, the exchange integral is given by  $J = (\pm)_{\text{bond}}(t/S\Delta)^2 J_{p-d}/2$ , where  $(\pm)_{\text{bond}}$  and  $J_{p-d}$  are the sign depending on the orthogonality for the p-d bonding and the transfer integral between p and d states, respectively [47]. In the case of  $\text{Ba}_2\text{La}_2\text{MW}_2\text{O}_{12}$ , the complicated crystal structure and the contribution of W 5d states to  $J$  makes this discussion difficult; however, at least the difference in the orthogonality of superexchange and super-superexchange pathways will be correlated with the inversion of sign of  $J$ . For  $\text{Ba}_2\text{La}_2\text{MnW}_2\text{O}_{12}$ , the  $pd\sigma$  bonding between Mn  $e$  states and O 2p states should play a key role in these magnetic interactions, while the  $pd\pi$  bonding between Ni  $t_2$  states and O 2p states is important for  $\text{Ba}_2\text{La}_2\text{NiW}_2\text{O}_{12}$ . Furthermore, because  $J$  is proportional to  $t$  to the 4th power, the increase in  $t$  is considered to be attributable to the enhancement of  $J$  and the magnetic ordering temperature for  $\text{Ba}_2\text{La}_2\text{NiW}_2\text{O}_{12}$ . In the case of  $\text{Ba}_2\text{La}_2\text{CoW}_2\text{O}_{12}$ , the magnetic interaction between Co ions will be in the competed states between those of the Mn and Ni compounds.

## Conclusions

The B-site defected 12L-perovskites  $\text{Ba}_2\text{La}_2\text{MW}_2\text{O}_{12}$  ( $\text{M} = \text{Mn}, \text{Co}, \text{Ni}, \text{Zn}$ ) having the two-dimensional triangular lattice of M ions were synthesized, and their crystal structures were refined by XRD and ND measurements. These results revealed that they adopt a structural model with a space group  $R\bar{3}$ , which is different from that in many earlier reports. The main differences between them are the layered cation ordering of A-site cations (Ba and La) and atomic positions of oxygen ions resulting in a small tilting of  $\text{MO}_6$  and  $\text{WO}_6$  octahedra along the  $c$ -axis. The  $\text{M} = \text{Co}$  and  $\text{Ni}$  compounds show a ferromagnetic ordering at 1.3 and 6.2 K, respectively, while the  $\text{Mn}$  compound are paramagnetic ( $T > 1.8$  K) with an antiferromagnetic interaction. The DFT calculations were carried out using the structural model ( $R\bar{3}$ ), and the calculated band gaps are comparable to the results of the UV-vis spectra. From the band structures, the magnetic interaction between M ions is varied by the hybridization between M 3d and O 2p states.

## Acknowledgement

This research was supported by Grant-in-aid for Scientific Research (C) (No. 15K05441, 16K05712) from the Japan Society for the Promotion of Science (JSPS). In addition, the ND experiment was approved by the Neutron Science Proposal Review Committee of J-PARC/MLF (Proposal No. 2016B0005) and supported by the Inter-University Research Program on Neutron Scattering of IMSS, KEK.

## References

- [1] M.F. Collins and O.A. Petrenko, *Can. J. Phys.*, **75**, 605–655 (1997).
- [2] H.T. Diep, *Frustrated Spin Systems* (World Scientific, Singapore, 2013).
- [3] P.W. Anderson, *Mater. Res. Bull.* **8**, 153–160 (1973).
- [4] L. Balents, *Nature.*, **464**, 199–208 (2010).
- [5] Y. Doi, Y. Hinatsu, and K. Ohoyama, *J. Phys.: Condens. Matter*, **16**, 8923–8935 (2004).
- [6] G. Blasse, *J. Inorg. Nucl. Chem.*, **27**, 993–1003 (1965).

- [7] V.U. Treiber and S. Kemmler-Sack, *Z. Anorg. Allg. Chem.*, **487**, 161–177 (1982).
- [8] Y. Shirata, H. Tanaka, , A. Matsuo, and K. Kondo, *Phys. Rev. Lett.*, **108**, 057205 1–5 (2012).
- [9] S. Nakatsuji, K. Kuga, K. Kimura, R. Satake, N. Katayama, E. Nishibori, H. Sawa, R. Ishii, M. Hagiwara, F. Bridges, T. U. Ito, W. Higemoto, Y. Karaki, M. Halim, A.A. Nugroho, J.A. Rodriguez-Rivera, M.A. Green, C. Broholm, *Science*, **336**, 559–563 (2012).
- [10] H.D. Zhou, E.S. Choi, G. Li, L. Balicas, C.R. Wiebe, Y. Qiu, J.R.D. Copley, and J.S. Gardner, *Phys. Rev. Lett.*, **106**, 147204 1–4 (2011).
- [11] J.G. Cheng, G. Li, L. Balicas, J.S. Zhou, J.B. Goodenough, C. Xu and H.D. Zhou, *Phys. Rev. Lett.*, **106**, 197204 1–4 (2011).
- [12] L. Katz and R. Ward, *Inorg. Chem.*, **3**, 205–211 (1964).
- [13] J.M. Longo, L. Katz, and R. Ward, *Inorg. Chem.*, **4**, 235–241 (1964).
- [14] S. Kemmler-Sack, *Z. Anorg. Allg. Chem.*, **453**, 163–165 (1979).
- [15] Von A. Fadini, S. Kemmler-Sack, H.J. Schittenhelm, H.J. Rother and U. Treiber, *Z. Anorg. Allg. Chem.*, **454**, 49–62 (1979).
- [16] Y. Torii, *Chem. Lett.*, **8**, 1393–1396 (1979).

- [17] S. Kemmler-Sack, *Z. Anorg. Allg. Chem.*, **461**, 142–145 (1980).
- [18] H.J. Rother, A. Fadini, and S. Kemmler-Sack, *Z. Anorg. Allg. Chem.*, **463**, 137–143 (1980).
- [19] H.J. Rother and S. Kemmler-Sack, *Z. Anorg. Allg. Chem.*, **465**, 179–182 (1980).
- [20] M. Herrmann and S. Kemmler-Sack, *Z. Anorg. Allg. Chem.*, **469**, 51–60 (1980).
- [21] M. Herrmann and S. Kemmler-Sack, *Z. Anorg. Allg. Chem.*, **470**, 113–117 (1980).
- [20] M. Herrmann and S. Kemmler-Sack, *Z. Anorg. Allg. Chem.*, **476**, 115–125 (1981).
- [21] M.A. Ryashentseva, A.A. Dulov, L.A. Abramova, O.P. Tkachenko, V.V. Fomichev, and A.E. Vetrov, *J. Cataly.*, **125**, 1–8 (1990).
- [24] Z. Li, J. Sun, L. You, Y. Wang, and J. Lin, *J. Alloys Compds.*, **379**, 117–121 (2004).
- [25] R. Yu, M. Li, N. Xie, T. Wang, N. Xue, *J. Am. Ceram. Soc.*, **98**, 3849–3855 (2015).
- [26] L. Yang, Y. Huang, H. Cheng, and H.J. Seo, *J. Phys. D: Appl. Phys.*, **48**, 435107 1–8 (2015).

- [27] R. Rawl, M. Lee, E.S. Choi, G. Li, K.W. Chen, R. Baumbach, C.R. dela Cruz, J. Ma, and H.D. Zhou, *Phys. Rev. B*, **95**, 174438 1–9 (2017).
- [28] Y. Shimoda, Y. Doi, Y. Hinatsu, and K. Ohoyama, *Chem. Mater.*, **20**, 4512–4518 (2008).
- [29] Y. Shimoda, Y. Doi, M. Wakeshima, and Y. Hinatsu, *J. Solid State Chem.*, **182**, 2873–2879 (2009).
- [30] Y. Shimoda, Y. Doi, M. Wakeshima, and Y. Hinatsu, *Inorg. Chem.*, **48**, 9952–9957 (2009).
- [31] K. Ohoyama, T. Kanouchi, K. Nemoto, M. Ohashi, T. Kajitani, Y. Yamaguchi, *Jpn. J. Appl. Phys.*, **37**, 3319–3326 (1998).
- [32] F. Izumi and K. Momma, *Solid State Phenom.*, **130**, 15–20 (2007).
- [33] R. Oishi, M. Yonemura, Y. Nishimaki, S. Torii, A. Hoshikawa, T. Ishigaki, T. Morishima, K. Mori, T. Kamiyama, *Nucl. Instrum. Methods Phys. Res. A*, **600**, 94–96 (2009).
- [34] R. Oishi-Tomiyasu, M. Yonemura, T. Morishima, A. Hoshikawa, S. Torii, T. Ishigaki, T. Kamiyama, *J. Appl. Crystallogr.*, **45**, 299–308 (2012).
- [35] K. Momma and F. Izumi, *J. Appl. Crystallogr.*, **41**, 653–658 (2008).
- [36] P. Blaha, K. Schwarz, G. Madsen, D. Kvasnicka, J. Luitz, *WIEN2k, An*

*Augmented Plane Wave+Local Orbitals Program for Calculating Crystal Properties, Techn.* (Universität Wien, Austria, Karlheinz Schwarz, 2001).

- [37] F. Tran, P. Blaha, *Phys. Rev. Lett.*, **102**, 226401 1–4 (2009).
- [38] R. Rawal, A.J. McQueen, L.J. Gillie, N.C. Hyatt, E.E. McCabe, K. Samara, N. McN. Alford, A. Feteira, I.M. Reaney, and D.C. Sinclair, *Appl. Phys. Lett.*, **94**, 192904 1–3(2009).
- [39] A.L. Chinelatto, K. Boulahya, D. Perez-Coll, U. Amador, C. Tabacaru, S. Nicholls, M. Hoelzel, D.C. Sinclair, G.C. Mather, *Dalton Trans.*, **44**, 7643–7653 (2015).
- [40] R.L. Carlin, *Magnetochemistry* (Springer, Berlin, 1986).
- [41] P. Kubelka, F. Munk, *Z. Techn. Phys.* **12**, 593–601 (1931).
- [42] J. Tauc, R. Grigorovici, A. Vancu, *Phys. Stat. Sol.*, **15**, 627–637 (1966).
- [43] K. Kopp, B.N. Harmon, S.H. Liu, *Solid State Commun.*, **22**, 677–679 (1977).
- [44] A. Hjelm, C.G. Granqvist, J.M. Wills, *Phys. Rev. B*, **54**, 2436–2445 (1996).
- [45] A. Kalinko, A. Kuzmina, R.A. Evarestov, *Solid State Commun.*, **149**, 425–428 (2009).
- [46] J. Zaanen, G.A. Sawatzky, *Can. J. Phy.*, **65**, 1262–1271 (1987).

- [47] J.B. Goodenough, *Magnetism and the Chemical Bond*, Interscience and John Wiley, N.Y. (1963).

## Figure captions

- Fig. 1 Powder X-ray diffraction profiles for (a)  $\text{Ba}_2\text{La}_2\text{NiW}_2\text{O}_{12}$  and (b)  $\text{Ba}_2\text{La}_2\text{ZnW}_2\text{O}_{12}$ . Upper and lower vertical marks mean the Bragg peak positions of main and impurity ( $\text{BaWO}_4$ ) phases, respectively.
- Fig. 2 Powder neutron diffraction profile for  $\text{Ba}_2\text{La}_2\text{NiW}_2\text{O}_{12}$ . Upper and lower vertical marks mean the Bragg peak positions of main and impurity ( $\text{BaWO}_4$ ) phases, respectively.
- Fig. 3 (a) XRD and (b) ND profiles calculated for  $\text{Ba}_2\text{La}_2\text{NiW}_2\text{O}_{12}$ . Black and red lines represent the profiles calculated by the space group  $R\bar{3}m$  and  $R\bar{3}$  with an ordered A-site arrangement, respectively, and blue line means the difference between them.
- Fig. 4 Time-of-flight powder neutron diffraction profile for  $\text{Ba}_2\text{La}_2\text{ZnW}_2\text{O}_{12}$ . Vertical marks mean the Bragg peak positions.
- Fig. 5 Schematic crystal structures of  $\text{Ba}_2\text{La}_2\text{MW}_2\text{O}_{12}$  and the comparison between two structural models: (a) space group  $R\bar{3}$  with an ordered A-site arrangement in this study and (b)  $R\bar{3}m$  with a disordered one in earlier reports. In lower illustrations, only one perovskite block ( $z = 0.54\text{--}0.79$ ) is drawn, and the red

lines mean the mirror ( $m$ ) planes.

Fig. 6 Temperature dependence of the reciprocal magnetic susceptibility for  $\text{Ba}_2\text{La}_2\text{MW}_2\text{O}_{12}$  ( $M = \text{Mn, Co, Ni, Zn}$ ). Solid lines mean the fitting curves by the Curie-Weiss law.

Fig. 7 Temperature dependence of the specific heat ( $C_p$ ) for  $\text{Ba}_2\text{La}_2\text{MnW}_2\text{O}_{12}$ . Inset shows the specific heat divided by temperature ( $C_p/T$ ) for  $\text{Ba}_2\text{La}_2\text{MnW}_2\text{O}_{12}$  (blue open circle) and  $\text{Ba}_2\text{La}_2\text{ZnW}_2\text{O}_{12}$  (red line) at low temperatures.

Fig. 8 Field dependence of the magnetization ( $M$ ) at 1.8 K for  $\text{Ba}_2\text{La}_2\text{MnW}_2\text{O}_{12}$  ( $M = \text{Mn, Co, Ni}$ ).

Fig. 9 Temperature dependence of the specific heat divided by temperature ( $C_p/T$ ) and magnetic entropy ( $S_{\text{mag}}$ ) for  $\text{Ba}_2\text{La}_2\text{CoW}_2\text{O}_{12}$ .

Fig. 10 Temperature dependence of the specific heat divided by temperature ( $C_p/T$ ) and magnetic entropy ( $S_{\text{mag}}$ ) for  $\text{Ba}_2\text{La}_2\text{NiW}_2\text{O}_{12}$ .

Fig. 11 Diffuse reflectance spectrum for (a)  $\text{Ba}_2\text{La}_2\text{ZnW}_2\text{O}_{12}$  and (b)  $\text{Ba}_2\text{La}_2\text{NiW}_2\text{O}_{12}$ . The Tauc plots are shown.

Fig. 12 (a) Energy dispersions and (b) the total and partial DOS for  $\text{Ba}_2\text{La}_2\text{ZnW}_2\text{O}_{12}$ . The zero energy is placed at the highest occupied state.

Fig. 13 (a) The total and partial DOS for  $\text{Ba}_2\text{La}_2\text{MnW}_2\text{O}_{12}$ . (b) Enlargement plot for the

partial DOS of Mn, W, O1, and O2. The zero energy is placed at the highest occupied state. (c) Spin density distributions in the central Mn ion and its ligands.

Fig. 14 (a) The total and partial DOS for  $\text{Ba}_2\text{La}_2\text{NiW}_2\text{O}_{12}$ . (b) Enlargement plot for the partial DOS of Ni, W, O1, and O2. The zero energy is placed at the highest occupied state. (c) Spin density distributions in the central Ni ion and its ligands.

Fig. 15 Schematic diagram of the band structure of  $\text{Ba}_2\text{La}_2\text{MW}_2\text{O}_{12}$ .

## Figures and Tables

Figure 1

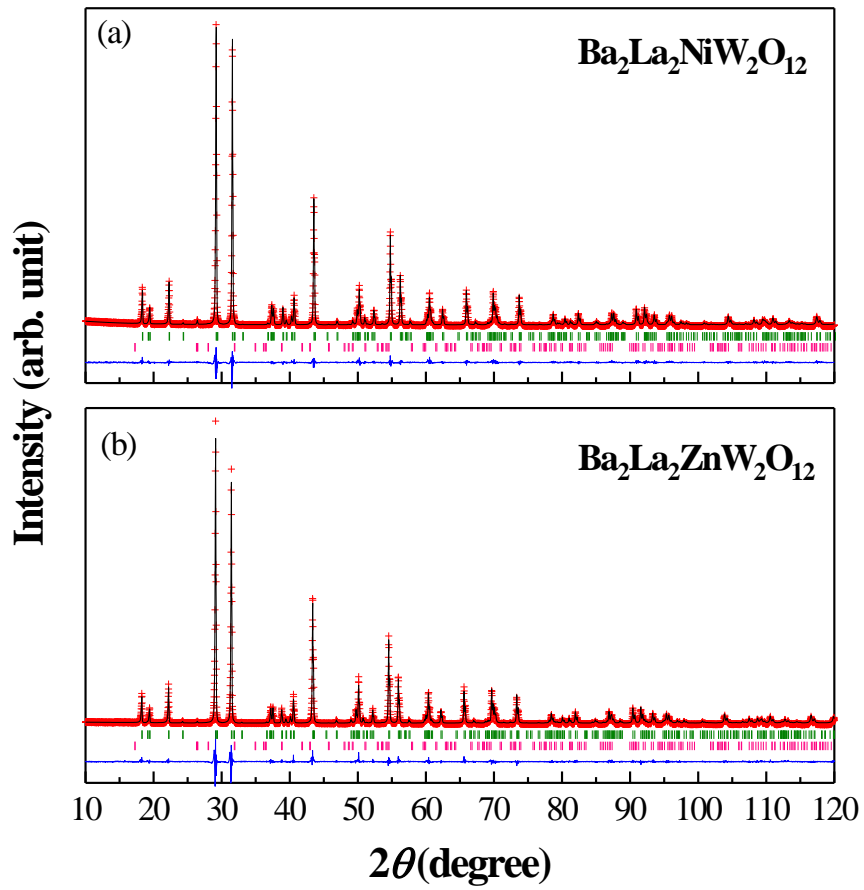


Figure 2

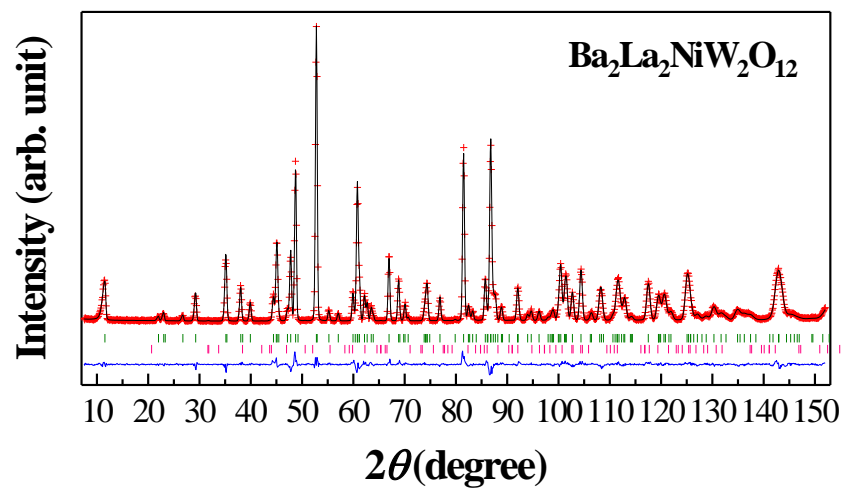


Figure 3

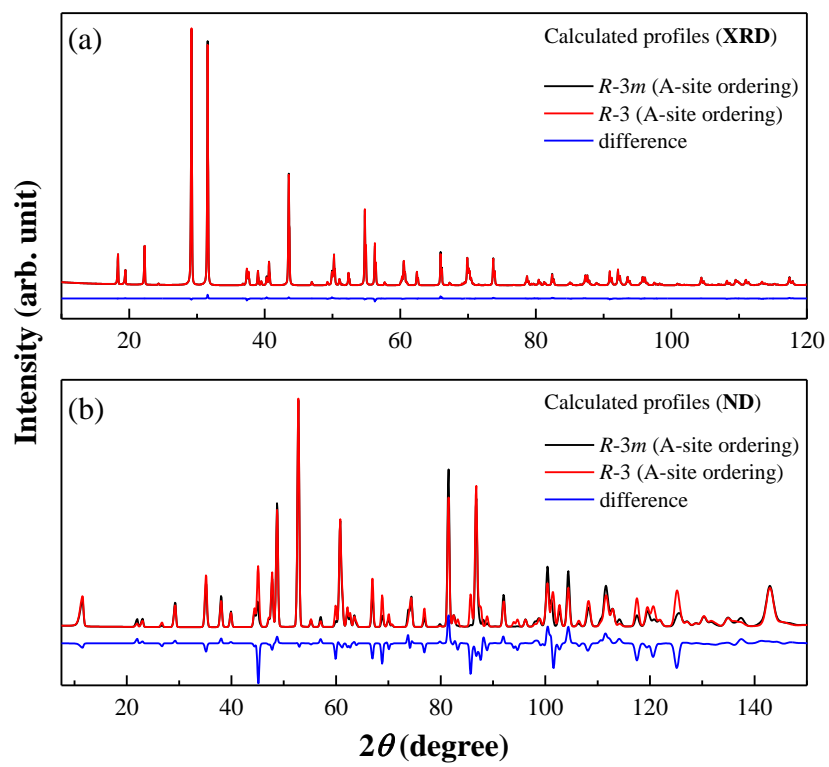


Figure 4

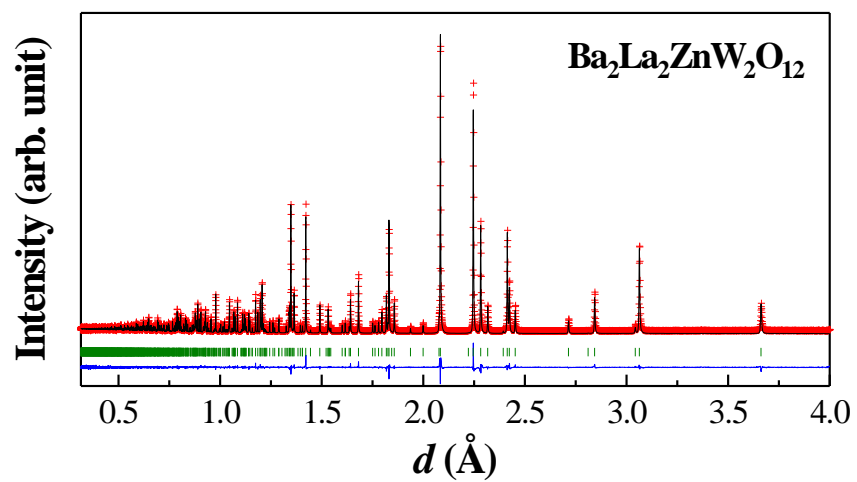


Figure 5

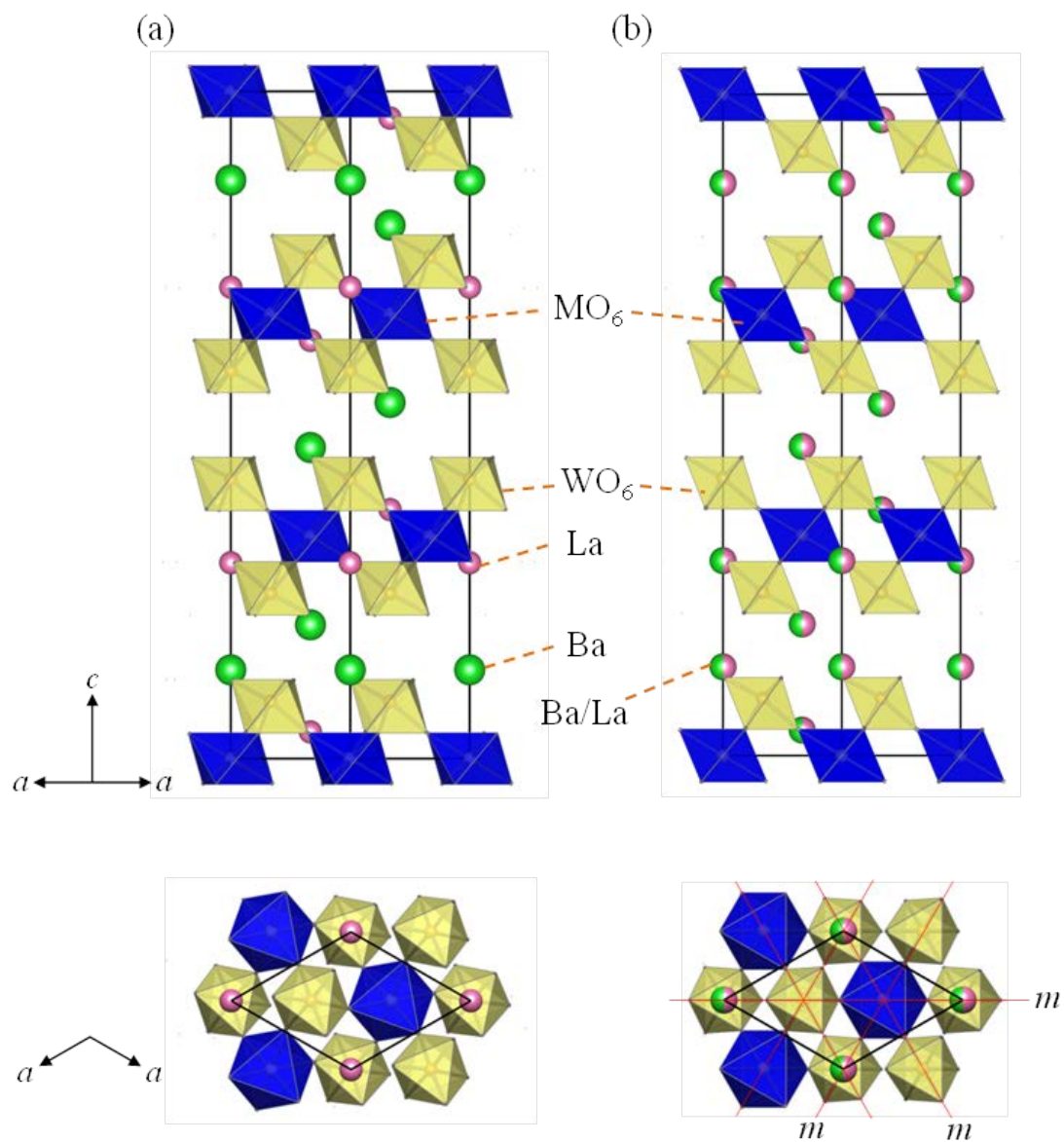


Figure 6

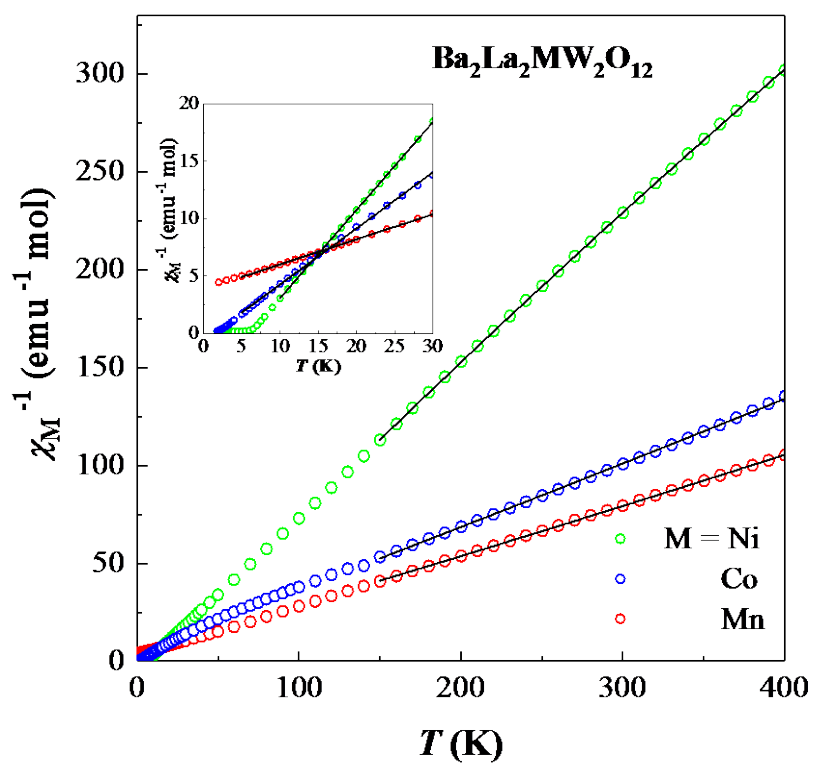


Figure 7

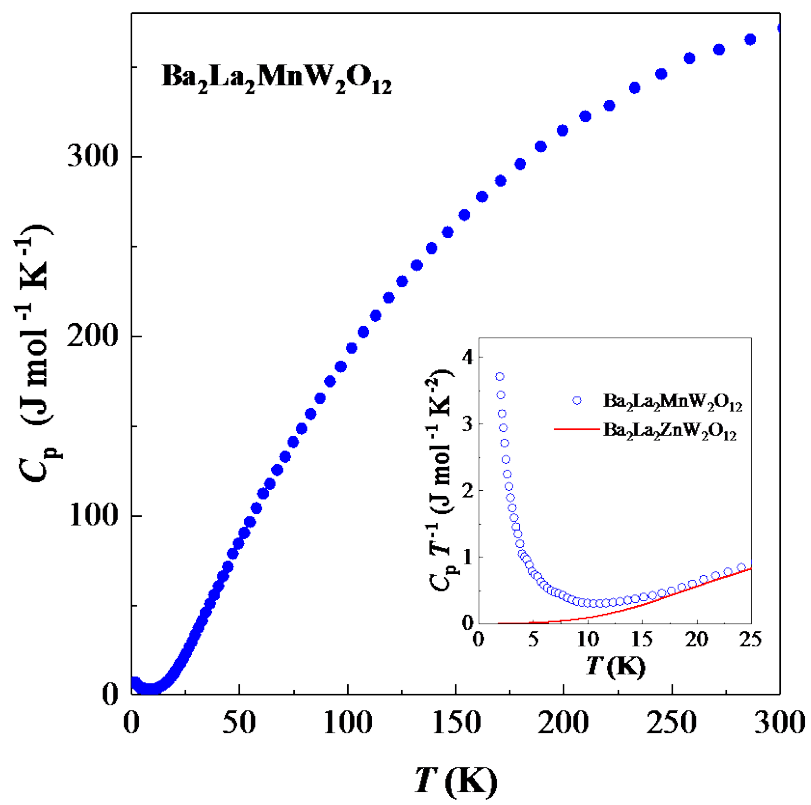


Figure 8

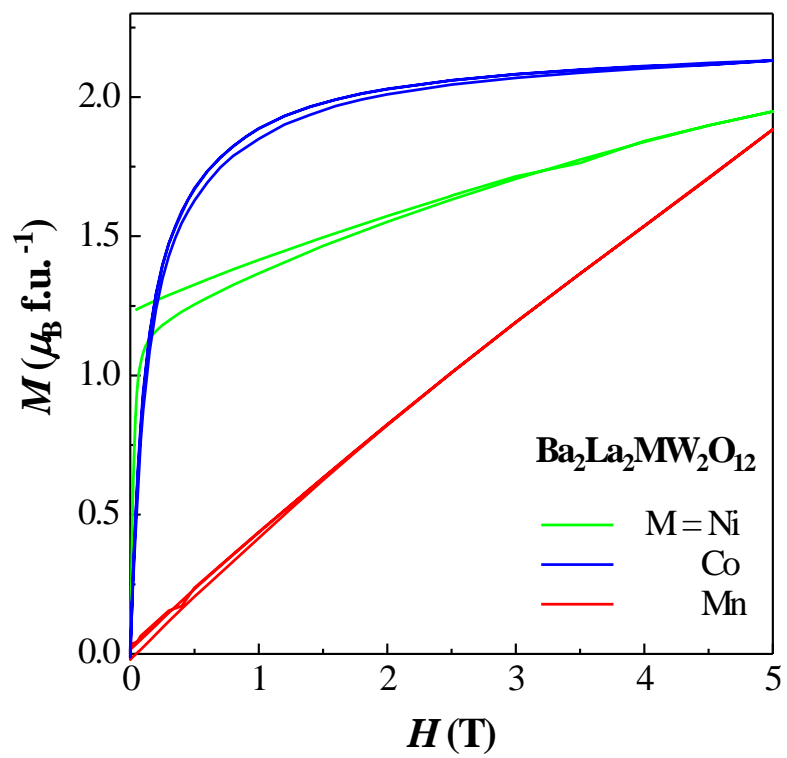


Figure 9

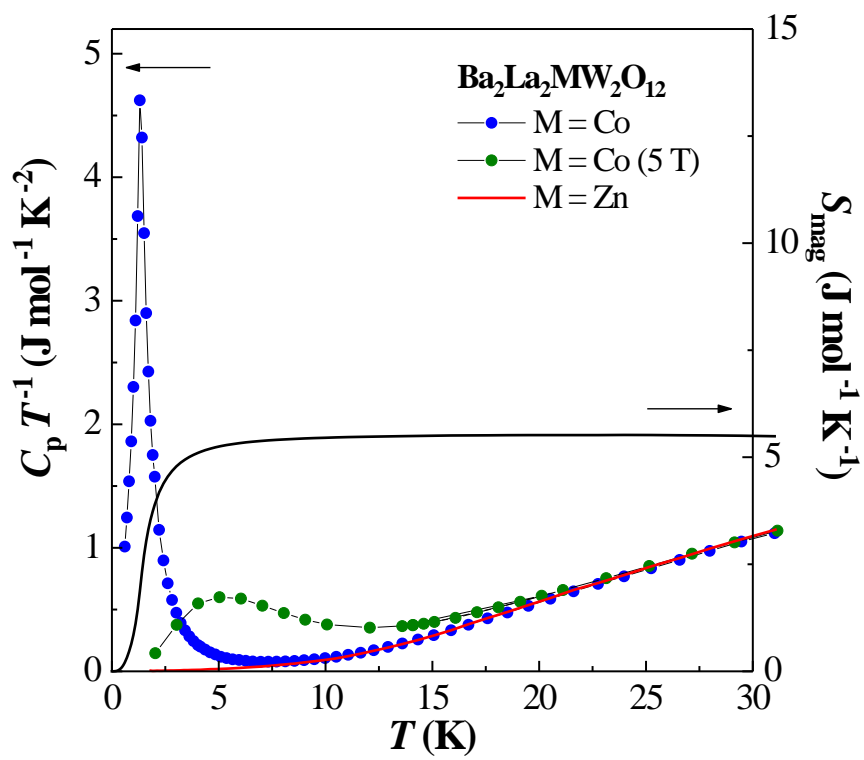


Figure 10

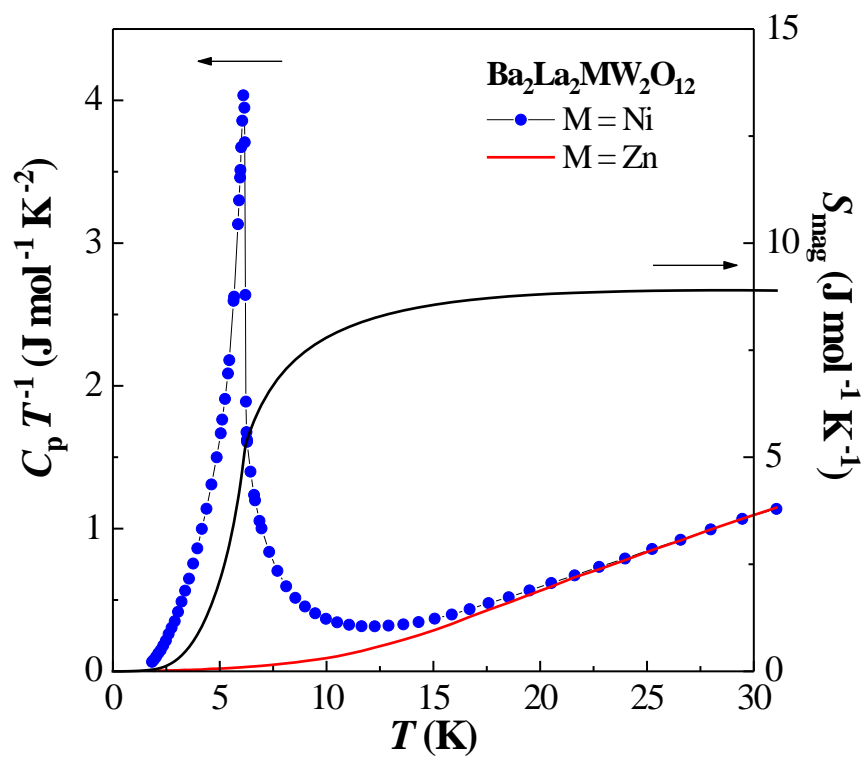


Figure 11

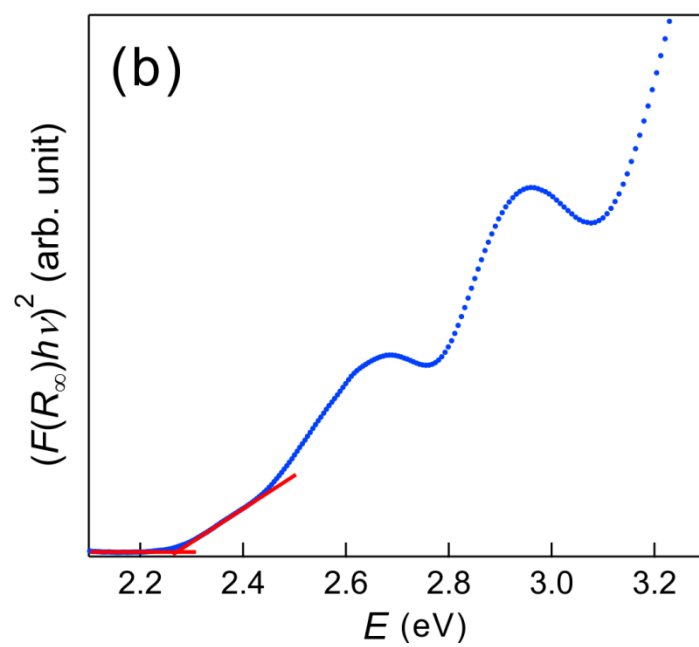
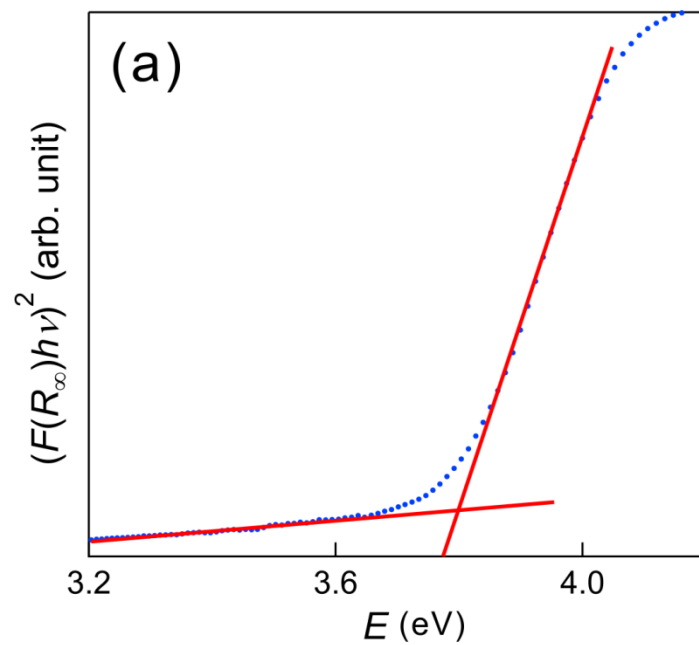


Figure 12

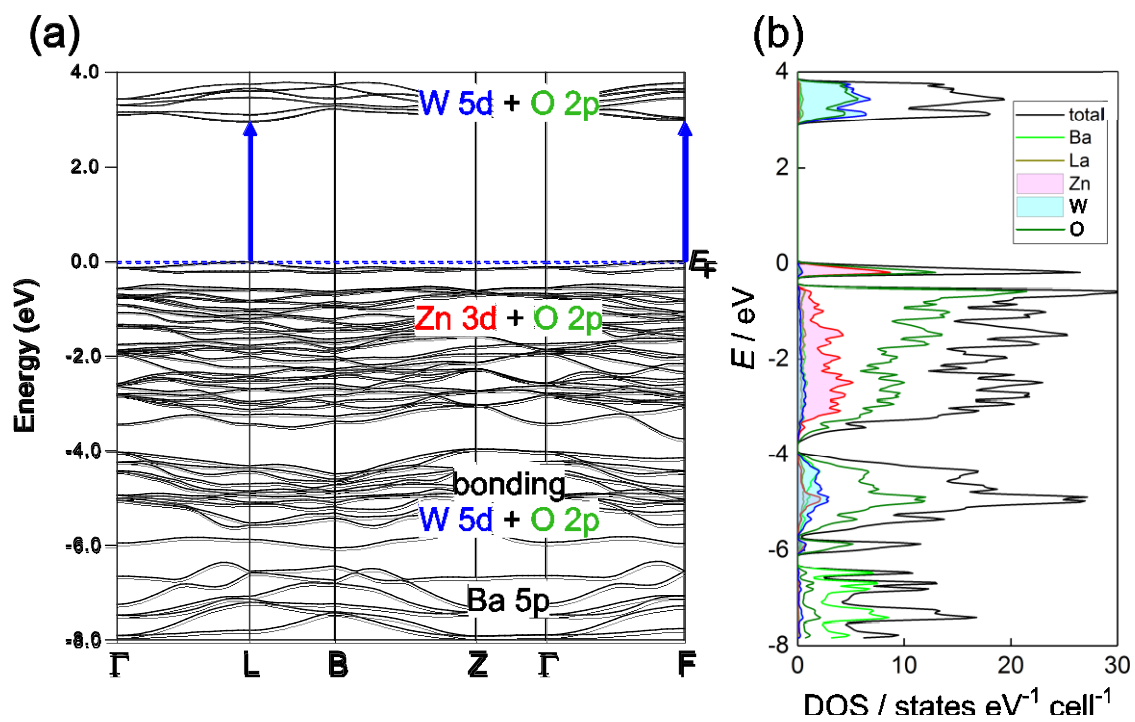


Figure 13

Figure 14

Figure 15

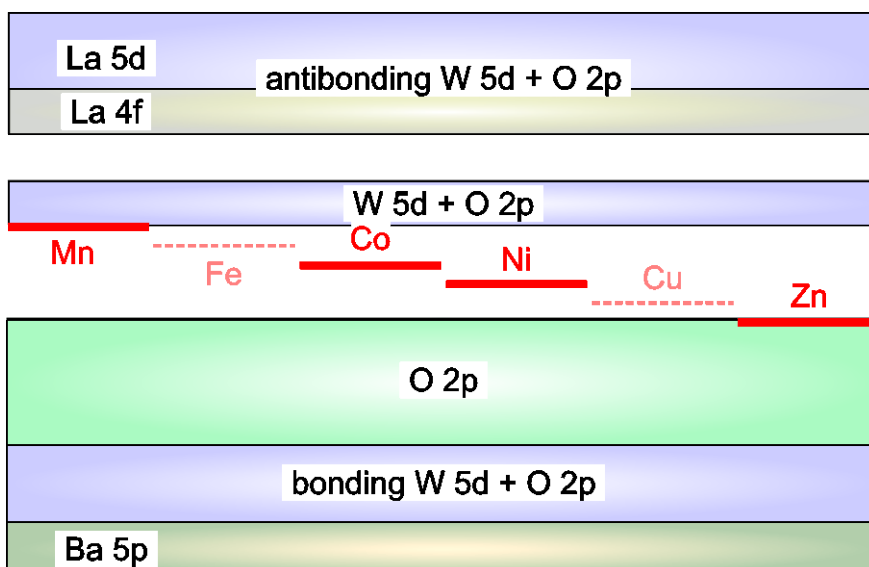


Table 1 Structural parameters for Ba<sub>2</sub>La<sub>2</sub>NiW<sub>2</sub>O<sub>12</sub> and Ba<sub>2</sub>La<sub>2</sub>ZnW<sub>2</sub>O<sub>12</sub> determined by the powder neutron diffraction measurement.

Atom	Site	<i>x</i>	<i>y</i>	<i>z</i>	<i>B</i> / Å <sup>2</sup>
<b>Ba<sub>2</sub>La<sub>2</sub>NiW<sub>2</sub>O<sub>12</sub></b>					
At room temperature, space group <i>R</i> -3;					
<i>a</i> = 5.6595(3) Å, <i>c</i> = 27.3387(13) Å,					
<i>R</i> <sub>wp</sub> = 5.74 %, <i>R</i> <sub>p</sub> = 4.56 %, <i>R</i> <sub>e</sub> = 3.21 %, <i>R</i> <sub>B</sub> = 1.15 %, <i>R</i> <sub>F</sub> = 0.55 %.					
Ba	6 <i>c</i>	0	0	0.13291(13)	0.36(8)
La	6 <i>c</i>	0	0	0.29346(9)	0.50(6)
Ni	3 <i>a</i>	0	0	0	0.44(7)
W	6 <i>c</i>	0	0	0.41889(14)	0.40(8)
O1	18 <i>f</i>	0.4644(4)	0.4705(5)	0.11809(6)	0.75(5)
O2	18 <i>f</i>	0.4319(4)	0.4559(5)	0.29479(8)	0.72(6)
<b>Ba<sub>2</sub>La<sub>2</sub>ZnW<sub>2</sub>O<sub>12</sub></b>					
At room temperature, space group <i>R</i> -3;					
<i>a</i> = 5.68687(1) Å, <i>c</i> = 27.39090(4) Å,					
<i>R</i> <sub>wp</sub> = 6.82 %, <i>R</i> <sub>p</sub> = 5.55 %, <i>R</i> <sub>e</sub> = 4.13 %, <i>R</i> <sub>B</sub> = 3.06 %, <i>R</i> <sub>F</sub> = 10.2 %.					
Ba	6 <i>c</i>	0	0	0.13331(3)	0.44(2)
La	6 <i>c</i>	0	0	0.29290(2)	0.53(1)
Zn	3 <i>a</i>	0	0	0	0.50(2)
W	6 <i>c</i>	0	0	0.41903(3)	0.25(1)
O1	18 <i>f</i>	0.46199(9)	0.46968(10)	0.11813(1)	0.75(1)
O2	18 <i>f</i>	0.42548(8)	0.45125(10)	0.29446(2)	0.81(1)

Table 2 Selected bond lengths (Å) and bond valence sums for Ba<sub>2</sub>La<sub>2</sub>NiW<sub>2</sub>O<sub>12</sub>.

	Ba <sub>2</sub> La <sub>2</sub> NiW <sub>2</sub> O <sub>12</sub>	Ba <sub>2</sub> La <sub>2</sub> ZnW <sub>2</sub> O <sub>12</sub>	Ba <sub>2</sub> La <sub>2</sub> MnW <sub>2</sub> O <sub>12</sub>	Ba <sub>2</sub> La <sub>2</sub> CoW <sub>2</sub> O <sub>12</sub>
	ND, RT	TOF-ND, RT	XRD, RT	XRD, RT
Ba–O1 × 3	2.677(2)	2.6819(5)	2.722(18)	2.697(14)
Ba–O1 × 3	2.805(3)	2.8090(8)	2.843(10)	2.818(8)
Ba–O1 × 3	3.041(2)	3.0663(5)	3.082(19)	3.048(14)
Ba–O2 × 3	3.134(4)	3.1530(8)	3.146(10)	3.187(8)
Average Ba–O	2.914(3)	2.9275(6)	2.948(14)	2.937(11)
BVS(Ba)	2.17	2.12	1.93	2.08
La–O2 × 3	2.515(2)	2.4965(4)	2.454(12)	2.453(10)
La–O2 × 3	2.645(3)	2.6713(6)	2.682(10)	2.610(8)
La–O2 × 3	2.716(3)	2.7181(6)	2.741(11)	2.689(8)
La–O1 × 3	3.150(2)	3.1968(6)	3.279(12)	3.240(10)
Average La–O	2.756(2)	2.7707(6)	2.789(11)	2.753(9)
BVS(La)	2.71	2.71	2.80	3.02
M–O2 × 6	2.068(2)	2.0939(5)	2.175(10)	2.145(8)
BVS(M)	1.96	2.09	2.12	1.77
W–O1 × 3	1.843(3)	1.8437(7)	1.822(10)	1.850(8)
W–O2 × 3	2.013(3)	2.0155(8)	1.976(10)	1.984(8)
Average W–O	1.928(3)	1.9296(7)	1.899(10)	1.917(8)
BVS(W)	5.98	5.96	6.43	6.11

Table 3 Effective magnetic moment( $\mu_{\text{eff}}$ ), Weiss constant( $\theta$ ) and transition temperature ( $T_N, T_C$ ) for  $\text{Ba}_2\text{La}_2\text{MW}_2\text{O}_{12}$ .

M	$\mu_{\text{eff}} / \mu_B$	$\mu_{M^{2+}} / \mu_B$ <sup>*1</sup>	$\theta / \text{K}$	$\theta_{\text{LT}} / \text{K}$	$T_N, T_C / \text{K}$ <sup>*2</sup>	Ref.
Mn	5.75(1)	5.92	-17.2(8)	-17.6(2)	< 1.8 (AF)	This study
	6.05	5.92	-16.6			[24]
	5.73	5.92	-10.7		1.7 (AF)	[27]
Co	5.08(1)	3.87	-17.1(9)	1.25(11)	1.3 (F)	This study
	5.19	3.87	-22.6	1.6	1.28 (F)	[27]
Ni	3.06(1)	2.83	13.1(3)	6.04(2)	6.2 (F)	This study
	3.19	2.83	25.5		6.2 (F)	[27]

Note. <sup>\*1</sup> magnetic moments of  $M^{2+}$  (spin-only values), <sup>\*2</sup> AF: antiferromagnetic, F: ferromagnetic